Monte Carlo Simulations of Spin Transport in Nanoscale InGaAs Field Effect Transistors

B. Thorpe,[1,*] K. Kalna,[2,†] F. C. Langbein,[3,‡] and S. Schirmer[1,§]

[1] *Department of Physics, College of Science, Swansea University, Singleton Park, Swansea, SA2 8PP, United Kingdom*

[2] *Electronic Systems Design Centre, College of Engineering, Swansea University, Bay Campus, Fabian Way, Swansea, SA1 8EN, United Kingdom*

[3] *School of Computer Science & Informatics, Cardiff University, 5 The Parade, Cardiff, CF24 3AA, United Kingdom*

(Dated: October 14, 2016)

By augmenting an in-house developed, experimentally verified Monte Carlo device simulator with a Bloch equation model with a spin-orbit interaction Hamiltonian accounting for Dresselhaus and Rashba couplings, we simulate electron spin transport in a 25 nm gate length InGaAs MOSFET. We observe non-uniform decay of the net magnetization between the source and gate electrodes and an interesting magnetization recovery effect due to spin refocusing induced by high electric field between the gate and drain electrodes. We demonstrate coherent control of the polarization vector of the drain current via the source-drain and gate voltages, and show that the magnetization of the drain current is sensitive to strain in the channel, suggesting that the device could act as a room-temperature nanoscale strain sensor.

Keywords: spin transport, Dresselhaus and Rashba spin-orbit couplings, strain sensor, Monte Carlo simulation, InGaAs FET

I. INTRODUCTION

Spin is one of the most intriguing quantum properties carried by elementary particles. Incorporating electron spin into the operation of semiconductor devices enables novel electronic devices [1, 2]. Among the most promising spin-based semiconductor devices are the spin field effect transistor (spinFET), considered a future candidate for high performance digital computing and memory with ultra low energy needs, and novel nanoscale quantum-enhanced sensor technology [3–6].

To realise spinFETs and similar devices exploiting spin degrees of freedom requires a thorough understanding of how electron spins interact in real semiconductor materials as well as the ability to control spin [7], which is essential to build devices with novel functionality and/or operation [8]. Although drift-diffusion models of spin transport have been very useful as a basis for simulations of spintronic devices [9], to understand how spin behaves in real nanoscale devices under realistic working conditions, one has to go beyond simple drift-diffusion models of electron spin transport by incorporating the electron spin degrees of freedom into self-consistent semiclassical or quantum transport device simulations. To this end, we apply finite-element quantum-corrected ensemble Monte Carlo simulations [10, 11] with electron spin to a nanoscale III-V field effect transistor to investigate spin transport within a realistically operating semiconductor device. The device we study is similar to the Datta-Das spin-FET [3], except that only the source electrode is ferromagnetic.

The simulation results suggest that the polarization of the electrons initially decays as they traverse the device as expected, but partially recovers as the electrons approach the drain. It appears that the electron spins are initially dephased but then partially refocused by the electric field of the gate electrode. As the drain electrode was deliberately chosen to be non-magnetic, the recovery of the magnetization cannot be attributed to existing polarized carriers inside the drain. It must be assumed to be due to partial rephasing of electron spins resulting in a net magnetization. Moreover, the decay and recovery depend on the gate voltage and can therefore be controlled. Our simulator also enables us to study the effect of strain on the spin transport. In particular, the Dresselhaus and Rashba effects depend on the direction and strength of the strain in the device, resulting in a change in electron polarization at the drain of the device. This could form the basis for nanoscale strain sensors in materials. Fig. 1 shows a 3D representation of our InGaAs MOSFET device and the spin polarization along the channel with and without strain.

This paper is organized as follows. In Section II, we briefly describe the simulations and the underlying theory. In Section III, we present and discuss the results of spin transport simulations for an unstrained $In_{0.3}Ga_{0.7}As$ MOSFET device including steady-state magnetization across the channel and the effect of the source-drain and gate voltages, respectively. In Section IV, the effect of microscopic strain is investigated based on $\vec{k}\cdot\vec{p}$ calculations to determine the strain dependence of the spin-orbit cou-

* ben4195@gmail.com

† http://engweb.swan.ac.uk/~karolkalna/; k.kalna@swansea.ac.uk

‡ frank@langbein.org; https://langbein.org/

§ sgs29@swan.ac.uk,lw1660@gmail.com; http://quantumcontrol.info/

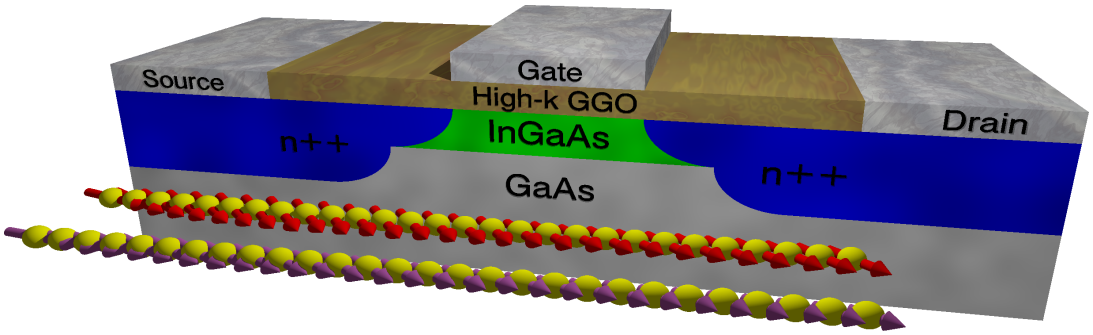

FIG. 1. 3D model of the studied $In_{0.3}Ga_{0.7}As$ MOSFET showing spin polarization of electrons along n-channel with 4% strain in the [001] direction (Red) and unstrained (Purple).

plings and its effect on spin transport and the observed magnetization of the drain current.

II. THEORY AND METHODS

The main simulation technique used in this work to model non-equilibrium many-body electron transport in realistic semiconductor devices is the ensemble Monte Carlo (MC) technique [12], which is self-consistently coupled with solutions of the Poisson equation (accounting for long-range electron-electron interactions) and quantum corrections using the effective quantum potential [13], all assembled in an in-house developed 2D finite element heterostructure MC device simulation tool [10, 14]. This device simulation tool was experimentally verified against numerous experimental results, including measured I-V characteristics of a 120 nm gate length $In_{0.2}Ga_{0.8}As$ pseudomorphic [15], lattice matched metamorphic HEMT [16], and a 50 mn gate length $In_{0.7}Ga_{0.3}As$/InP HEMT [17].

The MC engine considers three anisotropic valleys (Γ, L and X) with non-parabolic dispersion. The simulations consider the electron scattering with polar optical phonons, inter-valley and intra-valley optical phonons, non-polar optical phonons, acoustic phonons, interface roughness, interface phonons at the dielectric/semiconductor interface, and ionized impurity scattering using static screening. Furthermore, the alloy scattering as well as strain effects on bandgap, electron effective mass, optical phonon deformation potential, and energy are included in the device channel [14]. Details of the MC simulation tool can be found in [10, 17, 18]. This tool was adapted to include electron spin as a separate degree of freedom of the electrons using the spin density matrix $\rho_0(t)$ [19].

The spin state of a spin-$\frac{1}{2}$ particle such as an electron can be described by the density matrix

$$\rho_0(t) = \begin{pmatrix} \rho_{\uparrow\uparrow}(t) & \rho_{\uparrow\downarrow}(t) \\ \rho_{\downarrow\uparrow}(t) & \rho_{\downarrow\downarrow}(t) \end{pmatrix}, \tag{1}$$

where $\rho_{\downarrow\uparrow}(t) = \rho_{\uparrow\downarrow}(t)^*$ and $\rho_{\uparrow\uparrow}(t) + \rho_{\downarrow\downarrow}(t) = 1$. $\rho_{\uparrow\uparrow}$ and $\rho_{\downarrow\downarrow}$ represent the probability of finding the electron in either a spin up or spin down state and $\rho_{\uparrow\downarrow}$ / $\rho_{\downarrow\uparrow}$ represent the coherence.

The evolution of the spin states of individual electrons is governed by $\rho(t) = U(t)\rho_0 U(t)^\dagger$ where $U(t)$ is unitary propagator satisfying the Schrödinger equation

$$i\hbar\frac{d}{dt}U(t) = HU(t), \qquad U(0) = I. \tag{2}$$

Here $\hbar$ is the reduced Planck constant and H is the Hamiltonian operator of the system, which we take to be a spin-orbit interaction Hamiltonian consisting mainly of two terms: (i) the simplified Dresselhaus Hamiltonian [19]

$$H_D = \beta\langle k_y^2\rangle(k_z\sigma_z - k_x\sigma_x), \quad k_x^2, k_z^2 \ll \langle k_y^2\rangle, \tag{3}$$

which accounts for spin-orbit coupling as a result of bulk inversion asymmetry of the crystal, and (ii) the Rashba Hamiltonian

$$H_R = \eta(k_z\sigma_x - k_x\sigma_z), \tag{4}$$

which accounts for spin-orbit coupling due to structural inversion asymmetry of the quantum well. Here x is taken to be the transport direction along the device channel and y the growth direction of the quantum well. Discretizing the equations, we obtain the update rule for the density matrix,

$$\rho(t+\tau) = e^{-i(H_R+H_D)\tau/\hbar}\rho(t)e^{i(H_R+H_D)\tau/\hbar}. \tag{5}$$

Using basic matrix algebra it can easily be shown that

$$e^{-i(H_R+H_D)\tau/\hbar} = \begin{pmatrix} \cos(|\alpha|\tau) & i\frac{\alpha}{|\alpha|}\sin(|\alpha|\tau) \\ i\frac{\alpha^*}{|\alpha|}\sin(|\alpha|\tau) & \cos(|\alpha|\tau) \end{pmatrix} \tag{6}$$

with

$$\alpha = \hbar^{-1}[(\eta k_z - \beta\langle k_y^2\rangle k_x) + i(\eta k_x - \beta\langle k_y^2\rangle k_z)]. \tag{7}$$

This shows that the evolution of the spin polarization vector is equivalent to a rotation determined by the direction of the electron momentum. Our model neglects spin

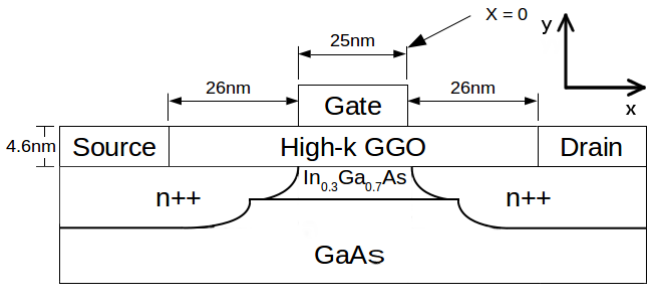

FIG. 2. Cross section of the 25 nm gate length, n-channel $In_{0.3}Ga_{0.7}As$ MOSFET.

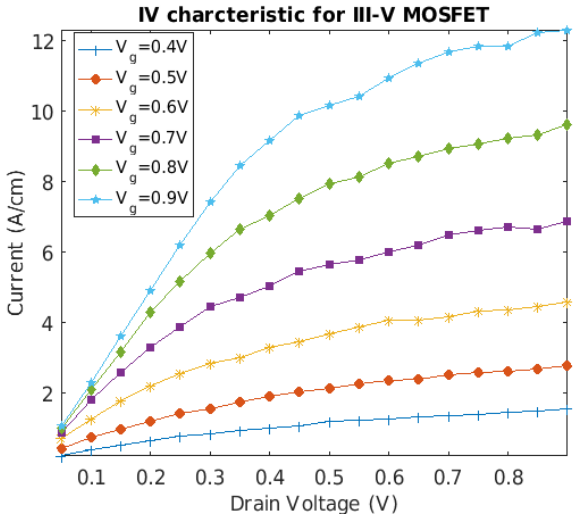

FIG. 3. $I_d - V_g$ characteristic of the 25 mn gate length InGaAs MOSFET.

flips due to impurity or phonon scattering, the Elliott-Yafet mechanism, and spin relaxation caused by hyperfine coupling, based on the observation that Dyakonov-Perel mechanism is the dominant source of spin relaxation in GaAs [8], although such effects could easily be incorporated into the simulator.

The spin polarization vector $\vec{s} = (s_x, s_y, s_z)^T$ is obtained from $s_\zeta(t) = \mathrm{Tr}(\sigma_\zeta \rho(t))$, where σ_ζ for $\zeta = x, y, z$ are the Pauli matrices

$$\sigma_x = \begin{pmatrix} 0 & 1 \\ 1 & 0 \end{pmatrix}, \quad \sigma_y = \begin{pmatrix} 0 & -i \\ i & 0 \end{pmatrix}, \quad \sigma_z = \begin{pmatrix} 1 & 0 \\ 0 & -1 \end{pmatrix}. \quad (8)$$

The components of the spin polarizsation vector of the current $S_\zeta = \langle s_\zeta(r,t) \rangle$ are obtained by averaging the components $s_\zeta(r,t)$ of the spin polarization vectors of all electrons in a thin slice through the device channel (along the direction of transport) located at position $x = r$ at time t. The magnitude $\|\vec{s}(r,t)\| \leq 1$ defines the amount of polarization, 1 being defined as 100% spin polarization in the direction of $\vec{s}(r,t)$.

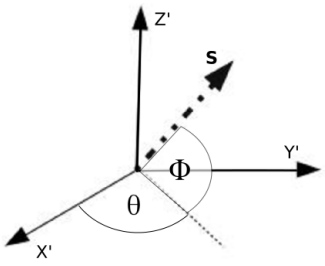

FIG. 4. Diagram showing the azimuthal (θ) and elevation (ϕ) angles used for the rotational analysis. The injection direction is mapped to the x' axis.

III. SPIN TRANSPORT IN NANOSCALE $In_{0.3}Ga_{0.7}As$ MOSFET

We simulate spin transport in an $In_{0.3}Ga_{0.7}As$ MOSFET with a gate length of 25 nm and a spacer of 26 nm at room temperature ($T = 300$ K) as shown in Fig. 2. This device consists of a 400 nm GaAs substrate, a 7 nm thick $In_{0.3}Ga_{0.7}As$ channel, a 4.6 nm layer of high-κ $Ga_2O_3/(Gd_xGa_{1-x})_2O_3$ (GGO, $\kappa = 20$) separating the channel from a metal gate with a work function of 4.05 eV. The structure has a background uniform p-type doping of $1 \times 10^{18}\,\mathrm{cm}^{-3}$ and n-type peak doping of $2 \times 10^{19}\,\mathrm{cm}^{-3}$ in the S/D contacts. The $I_d - V_g$ characteristics of the $In_{0.3}Ga_{0.7}As$ MOSFET are shown in Fig. 3 for comparison.

The source of the device was assumed to be ferromagnetic such that electrons injected from the source into the channel would be spin polarized. This process was assumed to be 100% efficient for the sake of simplicity. The electrons inside the channel were initialised such that there was no net magnetization across the channel. The simulation was then run with 100 000 super-particles with gate voltages of 0.5 V to 0.9 V and source-drain voltages of 0.5 V to 0.9 V, respectively in time steps of 1 fs for a total time of 10 ps. For each time step, the average polarization vector was calculated for the electrons contained in 100 evenly spaced slices across the channel. This entire process was repeated for three different injected polarizsations. This was achieved by setting the spin-polarization vector to be parallel to the x, y or z-axis upon injection into the channel from the source reservoir.

To better understand the coherent rotation of the magnetization vector, we map the Bloch vector for each injection case onto a common set of axes (denoted as x', y' and z') as shown in Fig. 4 and use spherical polar coordinates. The injection direction is mapped to the x' axis in all three cases and the two orthogonal directions define the azimuthal (θ) and elevation (ϕ) angles. This allows us to compare the rotation of the magnetization vector at the drain relative to its initial state for various injection directions and drain and gate voltages.

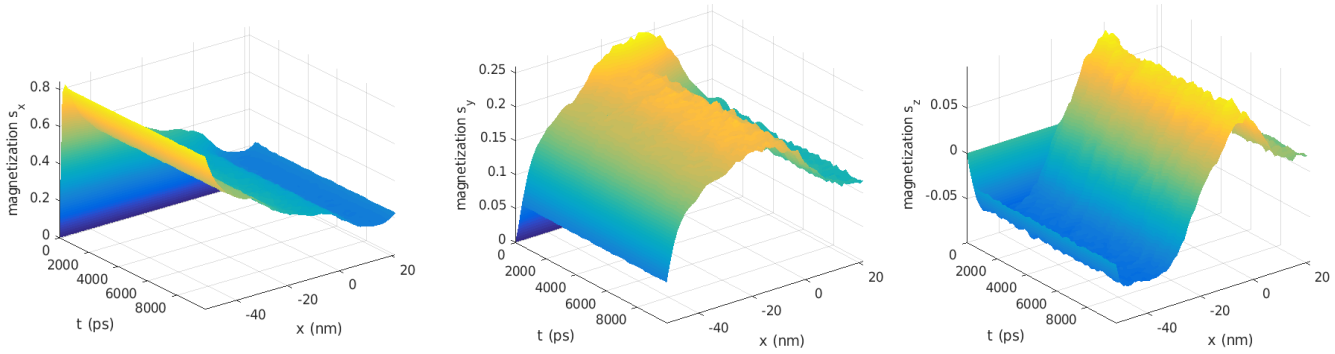

(a) x component of magnetization (b) y component of magnetization (c) z component of magnetization

FIG. 5. Spatiotemporal evolution of the components of the magnetization vector for injection of S_x-polarized spins with applied gate and source-drain voltages of 0.9 V each. x is the position along the channel with $x = 0$ being set at the end of the gate.

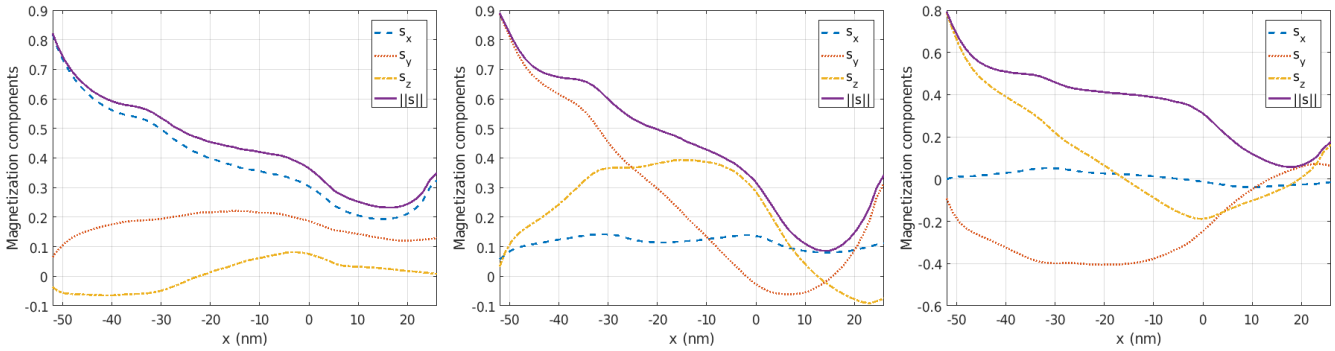

(a) Injection S_x-polarized. (b) Injection S_y-polarized. (c) Injection S_z-polarized.

FIG. 6. Components of magnetization vector vs position along the channel (averaged over 10 runs) taken at $t = 8$ ps, i.e., after a steady state was reached, for different injection polarizations at the same gate (V_g) and source-drain voltage (V_d) of 0.9 V.

A. Steady-State Magnetization along Channel

Fig. 5 shows that the components of the magnetization vector very quickly approach a steady state. Fig. 6 shows the evolution of components of the magnetization vector along the channel after a steady-state been reached for three different injection polarizations. In all three cases, the decay is not simply exponential, as might be expected based on simple drift-diffusion model simulations. In particular, we observe a magnetization recovery as we approach the channel region at the drain side, which is most pronounced when the injection polarization is in the S_y-direction, i.e., in the growth direction.

For x-polarized injection (Fig. 6a) we see a high S_x-polarization at the source-channel boundary ($x = -52$ nm, which decreases non-uniformly as we cross the channel from the source to the drain before recovering slightly between the right edge of the gate ($x = 0$ nm) and the drain, leading to a net magnetization at the left edge of the drain ($x = 26$ nm) of $\vec{s} = (0.36, 0.25, 0.08)$. Fig. 6b shows that the magnetization recovery is most prominent for the S_y injection case where the magnetization rises from a minimum of $S_y = 0.01$ at the right gate edge to $S_y = 0.28$ at the left drain edge.

The component resolved plots also show that the polarization vector of the current undergoes a coherent rotation as we move along the channel. For instance, in Fig. 6a, the initial fall in the S_x-magnetization is accompanied by an increase in the S_y-component, and later an increase in the S_z-component. As no external magnetic fields are applied, to directly rotate the spin polarization while the electrons are moving through the channel, this effect must be attributed to spin-orbit coupling.

Indeed, scatter plots of the x and z components of the Rasha and Dresselhaus spin-orbit coupling Hamiltonians

$$\begin{aligned}\vec{H}_R^{(n)} &= (\mathrm{Tr}(H_R\sigma_x), \mathrm{Tr}(H_R\sigma_y), \mathrm{Tr}(H_R\sigma_z)) \\ &= 2\eta(k_z, 0, -k_x), \\ \vec{H}_D^{(n)} &= (\mathrm{Tr}(H_D\sigma_x), \mathrm{Tr}(H_D\sigma_y), \mathrm{Tr}(H_D\sigma_z)) \\ &= 2\beta\langle k_y^2\rangle(-k_x, 0, k_z)\end{aligned}$$

show that there is less scattering for the particles in the gate region for the nth particle versus the x-position in the channel in Figs. 7a and 7c, for one run of the Monte Carlo simulator with $V_g = 0.9$ V and $V_d = 0.5$ V and 100,000 particles. Furthermore, vector plots of the respective single-electron Rashba and Dresselhaus Hamiltonian vectors averaged over all particles in thin slices along the channel (Figs. 7b and 7d) shows that the average Hamiltonians are small away from the gate, but large

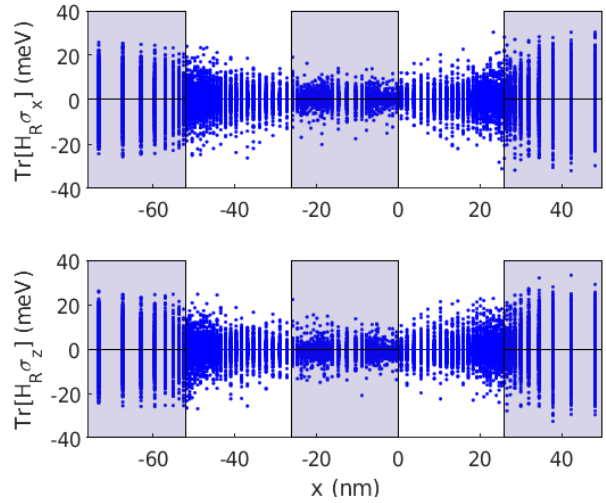

(a) Rashba Field $\vec{H}_R$ Scatter Plot

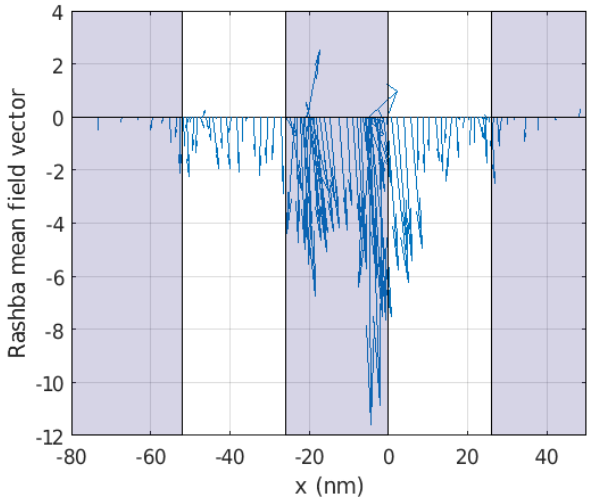

(b) Rashba Field $\vec{H}_D$ Vector Plot

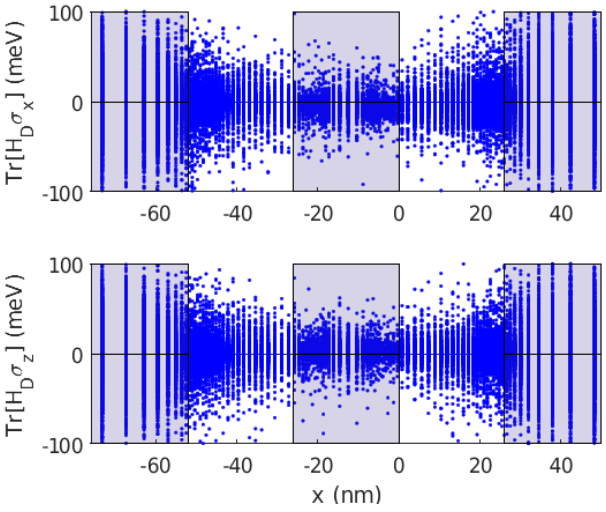

(c) Dresselhaus Field $\vec{H}_D$ Scatter Plot

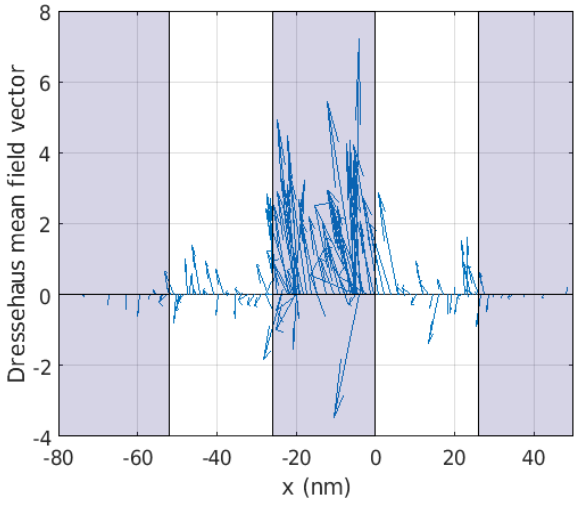

(d) Dresselhaus Field $\vec{H}_D$ Vector Plot

FIG. 7. Scatter plot of x and z components of single electron Rashba and Dresselhaus Hamiltonians $\vec{H}_R$ and $\vec{H}_D$ vs position of electron in the channel for a single Monte Carlo run ($V_g = 0.9\,\mathrm{V}, V_d = 0.5\,\mathrm{V}$) showing magnitude and distribution (left), and corresponding Hamiltonian vectors averaged over all particles in thin slices along the channel direction x (right). Shading indicates the position of the electrodes.

in the gate region. This suggests that the spin-orbit coupling away from the gate mostly imparts random kicks to the electron spins resulting in dephasing. However, in the gate region, the strong electric field of the gate causes the spin-orbit coupling to act more like a coherent rotation of the electron spins.

B. Gate Voltage Dependence

Fig. 8 shows the total magnetization after a steady-state has been reached for different gate voltages. It suggests that lower gate voltages initially lead to faster magnetization decay. The effect is most pronounced for S_x-polarized injection (see Fig. 8a). A possible explanation for this effect is that larger gate voltages induce a high fringing electric field resulting in the electrons experiencing more acceleration. Electrons thus reach the gate faster and under fewer scattering events. However, the situation is more complicated for the final magnetization at the drain edge due to the magnetization recovery between the gate and drain. This recovery is more pronounced for lower gate voltages, possibly due to slower moving electrons experiencing less deceleration as they move toward the drain, giving the magnetization more time to recover.

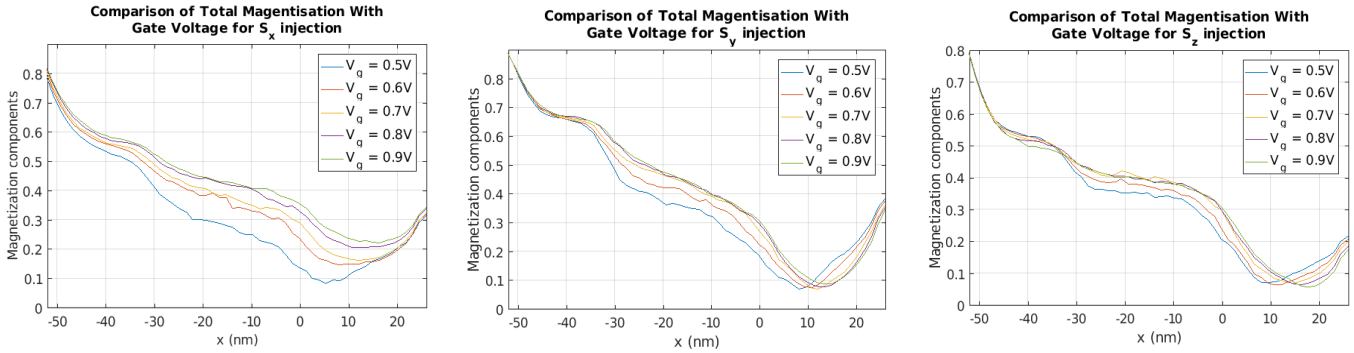

(a) Injection x-polarized. (b) Injection y-polarized. (c) Injection z-polarized.

FIG. 8. Total magnetization versus position along the channel after steady-state has been reached at different gate voltages (V_g) and a fixed source-drain voltage (V_d) of 0.9 V.

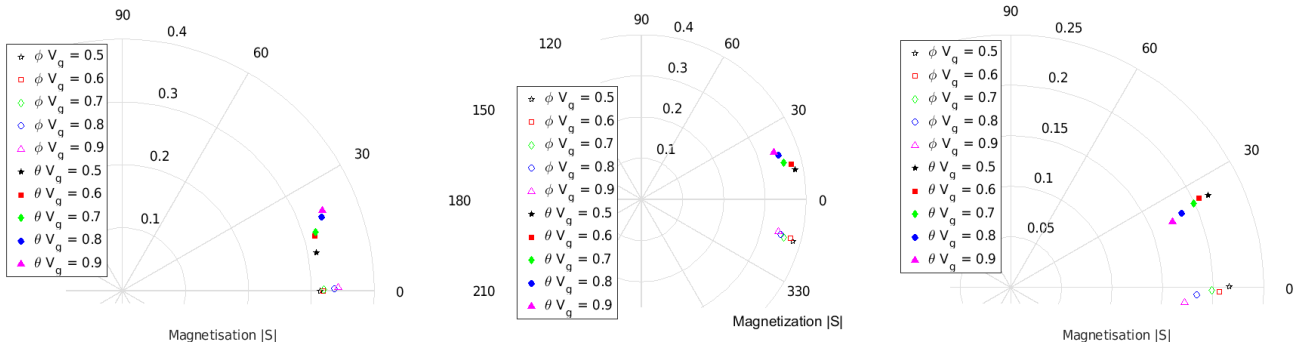

(a) Injection x-polarized. (b) Injection y-polarized. (c) Injection z-polarized.

FIG. 9. Polar plot of total magnetization vector at left drain edge ($x = 25$ nm) for varying gate voltages from 0.5 V to 0.9 V and fixed source drain voltage 0.9 V. Filled shapes indicate azimuthal angle θ and open shapes the elevation angle ϕ.

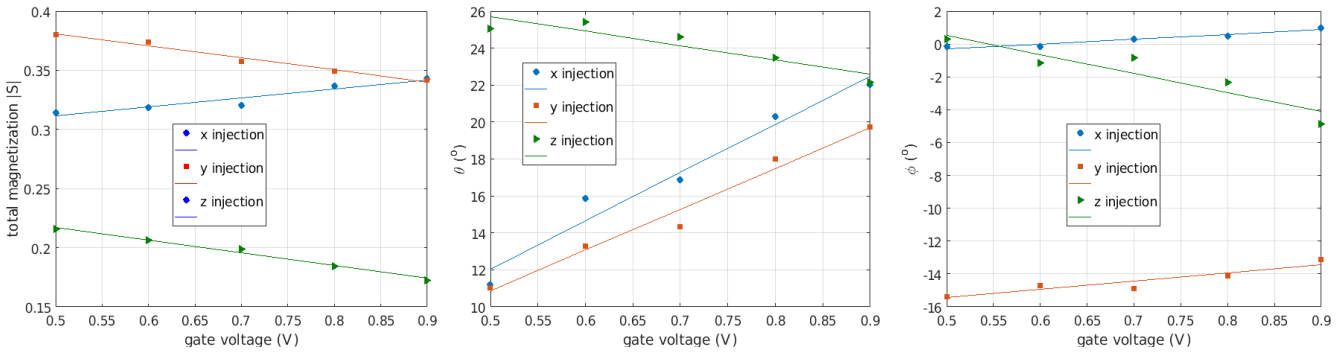

(a) Total Magnetization (b) θ angle (c) ϕ angle

FIG. 10. Magnetization at left drain edge ($x = 25$ nm) as a function of gate voltage for fixed source drain voltage of 0.9 Vwith linear regression fits to elucidate general trends.

Fig. 9 shows the azimuthal and elevation angles of the magnetization vector at the drain edge, relative to the injection polarization for different gate voltages. Fig. 10a shows that the total magnetization at the drain edge is linearly decreasing with the gate voltage for S_y and S_z-polarized injection, while for S_x-injection there is a slight net increase with increasing gate voltage. Fig. 10b further shows that the azimuthal angle θ, indicating a rotation in the S_x-S_y plane, increases linearly with the applied gate voltage for both S_x and S_y-injection while it decreases for S_z-injection. For S_z-injection the azimuthal rotation angle is greater but less sensitive to the gate voltage. Fig. 10c shows that the elevation angle ϕ is almost constant as a function of gate voltage for S_x and S_y-injection, but decreases linearly for z-injection.

The differences in the observed coherent rotation of the magnetization as a function of the applied voltages can be partially explained by changes in the strength of the spin-

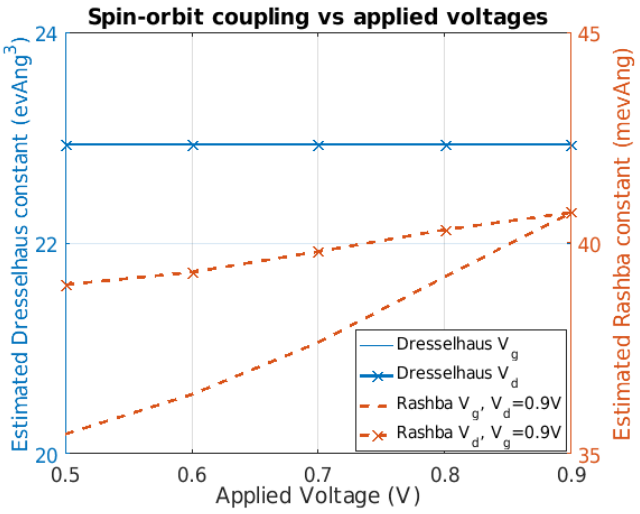

FIG. 11. Dependence of Rashba and Dresselhaus coupling on source-drain and gate voltage.

orbit coupling. Fig. 11 shows that the Rashba coupling constant increases with the applied voltages, while the Dresselhaus constant is independent of the voltages.

C. Source-Drain Voltage Dependence

Fig. 12 shows the total magnetization after a steady-state has been reached for different source-drain voltages and fixed gate voltage of 0.9 V. The latter value was chosen as the conventional 25 nm gate length MOSFET for digital applications would have to operate at $V_d = V_g - V_{\text{th}} = 0.9\,\text{V}$. It suggests that varying the source-drain voltage for a fixed gate voltage does not change the initial rate of magnetization decay between the source and the gate but affects the magnetization recovery between the gate and the drain.

Fig. 13 shows the azimuthal and elevation angles of the magnetization vector at the drain edge, relative to the injection polarization for different source-drain voltages in a polar plot. Fig. 14a shows the total magnetization and as well as its relative orientation at the left drain edge, again after a steady-state has been reached, as a function of the source-drain voltage. Both figures suggest a moderate decrease in the total magnetization at the drain edge with increasing source-drain voltage when the gate voltage is kept fixed at 0.9 V, especially for S_x and S_y injection. The total magnetization at the drain edge is much lower for S_z-injection than for S_x or S_y injection and effectively independent of the source-drain voltage. Fig. 14b further suggests a linear decrease in the azimuthal rotation angle for S_x and S_y, while for the S_z-injection the values scatter around 21.5°. Fig. 14c suggests that the elevation angle ϕ is almost independent of the source-drain voltage for a fixed gate voltage of $V_g = 0.9\,\text{V}$ for S_z-injection, but shows a linear decrease for the S_x and S_y injections.

Although the amount of variation in the observed rotation of the magnetization vector as a function of the source-drain and gate voltages is not huge, the simulation results suggest that a certain amount of coherent control of the magnetization vector is possible by adjusting the gate and source-drain voltages alone, without any need for external magnetic fields. The sensitivity to voltage changes also exhibits a dependence on the injection polarization.

IV. EFFECT OF STRAIN ON SPIN TRANSPORT

Mechanical strain alters the amount of Dresselhaus coupling by changing the symmetry of the bulk crystal and the quantum well. Thus, application of strain could theoretically be a way to control the amount of spin-orbit coupling and the magnetization at the drain. Alternatively, measuring the magnetization of the drain current could enable us to indirectly measure mechanical strain in the device and form the basis for a nanoscale mechanical strain sensor. To gain a better understanding of the effects of mechanical strain on the values of η and β, we calculate the electronic bandstructures of our device as a function of mechanical strain. To this end we use the $\vec{k}\cdot\vec{p}$ method as it provides a good trade-off between efficiency and accuracy for bandstructure calculations for bulk semiconductors and heterostructures [20–22].

A. The k · p Method

The method consists of calculating the band structure in the vicinity of a given point in reciprocal-space for which the band structure is known using the perturbation theory. The use of this technique was first proposed by Kane in 1957 [22] and included the lowest conduction band (Γ_{6c}) alongside the light hole, heavy hole (Γ_{8v}) and split off (Γ_{7v}) valence bands. This has since been extended to include up to as many as 40 bands and can be easily adapted to include the effects of spin-orbit coupling and strain [21]. In our case we only need to consider 7 bands (14 with the inclusion of a spin), which is achieved by including the next two conduction bands (the doublet Γ_{7c} and quadruplet Γ_{8c} bands).

The Hamiltonian for this system is constructed following the procedure used by Pfeffer and Zawadzki [23, 24]. We start with the general Schrödinger equation for an electron wave function ψ_k with a wavevector $\vec{k}$,

$$\begin{aligned}[H + V(r)]\psi_k(r) &= E(k)\psi_k(r),\\ H &= \frac{p^2}{2m_0} + \frac{\hbar}{4m_0^2c^2}(\sigma\times\nabla V)\cdot\vec{p},\end{aligned} \tag{9}$$

where σ represents the vector of Pauli matrices and $V(r)$ is a periodic potential. We look for solutions to Eq. (9)

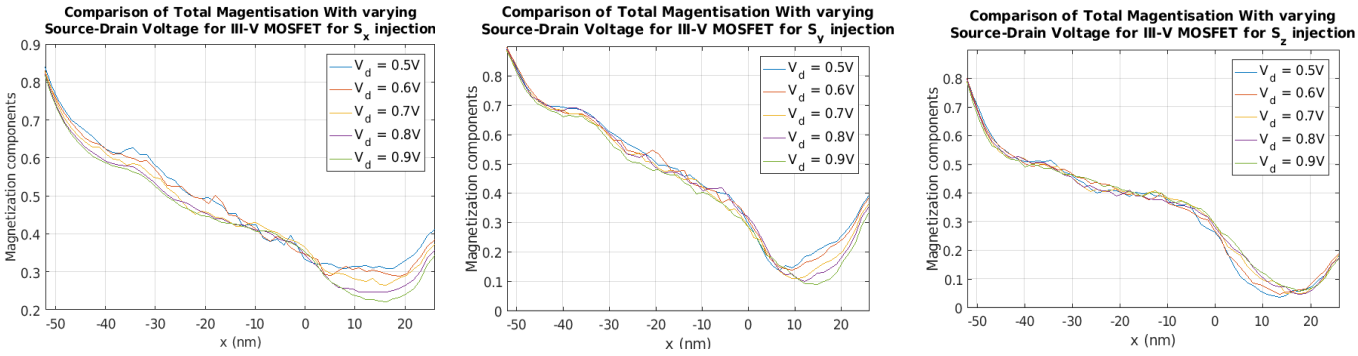

(a) Injection S_x-polarized. (b) Injection S_y-polarized. (c) Injection S_z-polarized.

FIG. 12. Total magnetization versus position along the channel after steady state has been reached at different source-drain voltages and a fixed gate voltage of 0.9 V.

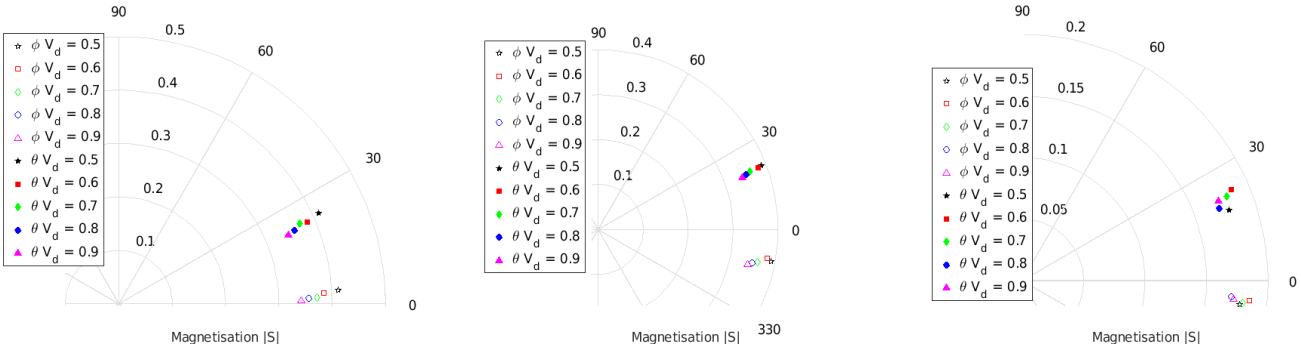

(a) Injection S_x-polarized. (b) Injection S_y-polarized. (c) Injection S_z-polarized.

FIG. 13. Polar plot of total magnetization vector at left drain edge ($x = 25\,\text{nm}$) for varying source drain voltages from 0.5 V to 0.9 V and fixed gate voltage 0.9 V. Filled shapes indicate azimuthal angle θ and open shapes the elevation angle ϕ.

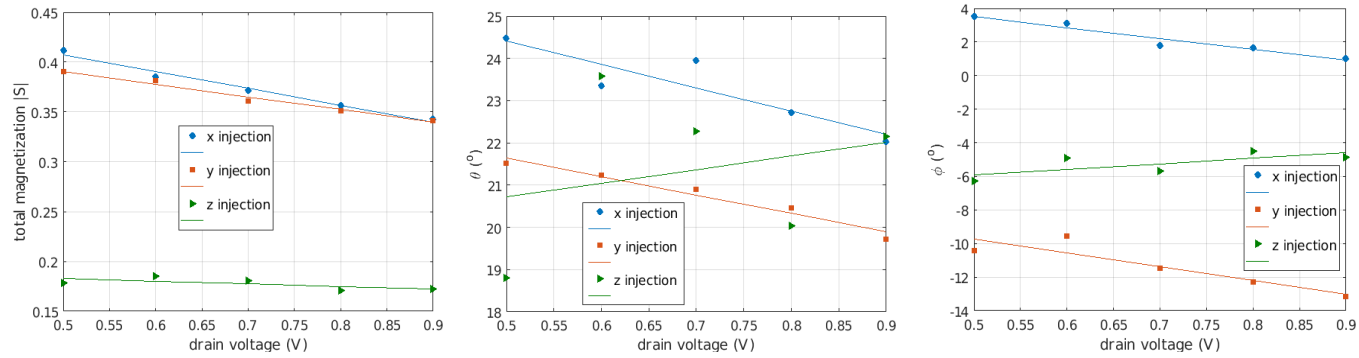

(a) Total Magnetization (b) θ angle (c) ϕ angle

FIG. 14. Magnetization at the left drain edge ($x = 25\,\text{nm}$) as a function of source-drain voltage for a fixed gate voltage of 0.9 V with linear regression fits to elucidate general trends in the data.

of Luttinger-Kohn form [25],

$$\psi_k^m(r) = e^{ik\cdot r}\sum_l c_l^m u_l(r), \tag{10}$$

where the summation is over all bands and the index m indicates the band of interest. The L-K periodic amplitudes satisfy Eq. (9) at a band's extremity ($k = 0$ in our case) and are orthonormal such that $\left(\frac{1}{\Omega}\right)\langle u_{i'}|u_l\rangle = \delta_{l'l}$ where Ω is the unit cell over which the integration is taking place. Thus, by substituting Eq. (10) into Eq. (9), multiplying the left hand side by $\left(\frac{1}{\Omega}\right)u(r)^*$ and integrating over the unit cell, we obtain

$$\sum_l \left[(E^{(l)} + \frac{\hbar^2k^2}{2m_0} - E)\delta_{l'l} + \frac{\hbar}{m_0}k\cdot p_{l'l} + H^{s.o}_{l'l}\right]c_l^m = 0, \tag{11}$$

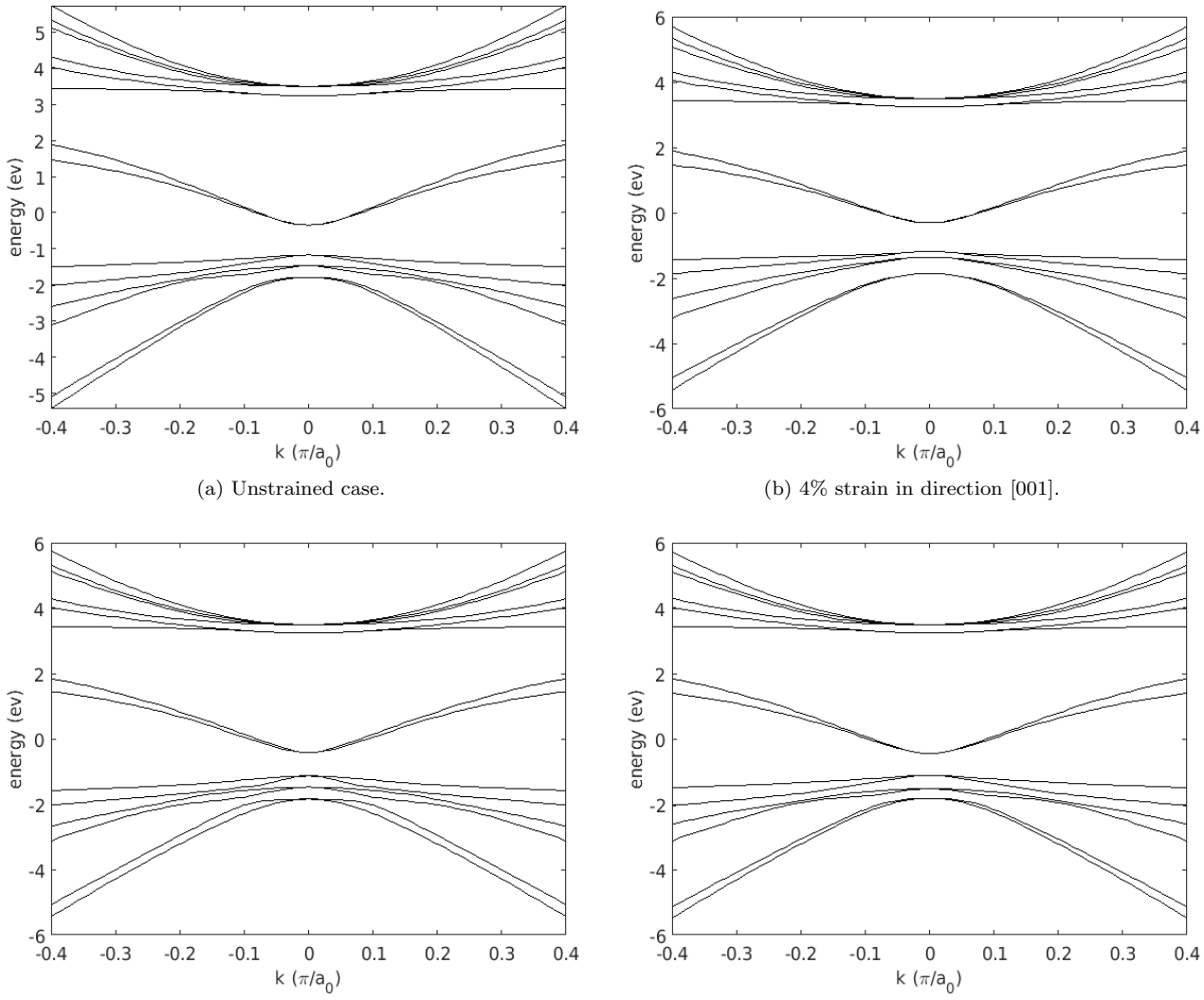

(a) Unstrained case.

(b) 4% strain in direction [001].

(c) 4% strain in direction [110].

(d) 4% strain in direction [111].

FIG. 15. Band structures for $In_{0.3}Ga_{0.7}As$ calculated using $\vec{k} \cdot \vec{p}$ method with different mechanical strain.

where the index l' runs over all the bands, $E^{(l)}$ is the band energy and $p_{l'l}$ represents the inter-band matrix elements.

Finally, we must account for the effects of the interactions with far-level bands. This is achieved by using the method developed by Lowdin [26, 27], which uses a combination of perturbation theory for the quasi-degenerate levels and the far-levels. Several additional Hamiltonian parameters are required to account for this. We use the procedure outlined in Pfeffer and Zawadzki [24], which includes the diagonal contributions to the conduction Γ_{6_c} band, the contributions to the Luttinger valence γ^l parameters, and the linear k terms, while all other far-level terms are neglected for simplicity. We use γ_i to represent the modified Luttinger parameters, where the $\vec{k} \cdot \vec{p}$ interaction of the Γ_{8v} level with the Γ_{6c}, Γ_{8c} and Γ_{7c} levels are subtracted, since they are included explicitly in the matrix.

With this in mind, we construct the Hamiltonian for the system by careful selection of basis functions for each band of interest, defined in Table I. These basis functions are chosen deliberately to exploit orbital symmetries as for III-V semiconductors the Γ_{6c} conduction band consists of electrons from s-type orbitals while the valence bands Γ_{8v} and Γ_{7v} and the two remaining conduction bands Γ_{8c} and Γ_{7c} consist of electrons from p-type orbitals and only inter-band interactions of opposite parity will produce non-zero results. Thus we greatly reduce the number of parameters needed to calculate the band structure such that the only non-zero momentum matrix

Band	Basis function	Energy
Γ_{6c}	$\lvert S\uparrow\rangle$	0
	$\lvert S\downarrow\rangle$	0
Γ_{8v}	$-\frac{1}{2}\lvert(X+iY)\uparrow\rangle$	$-E_0$
	$\frac{1}{2}\lvert(X+iY)\downarrow\rangle$	$-E_0$
	$\sqrt{\frac{2}{3}}\lvert Z\uparrow\rangle-\frac{1}{\sqrt{6}}\lvert(X+iY)\downarrow\rangle$	$-E_0$
	$\sqrt{\frac{2}{3}}\lvert Z\downarrow\rangle+\frac{1}{\sqrt{6}}\lvert(X+iY)\uparrow\rangle$	$-E_0$
Γ_{7v}	$-\frac{1}{\sqrt{3}}\lvert Z\uparrow\rangle-\frac{1}{\sqrt{3}}\lvert(X+iY)\downarrow\rangle$	$-(E_0+\Delta_0)$
	$\frac{1}{\sqrt{3}}\lvert Z\downarrow\rangle-\frac{1}{\sqrt{3}}\lvert(X+iY)\uparrow\rangle$	$-(E_0+\Delta_0)$
Γ_{8c}	$-\frac{1}{2}\lvert(X'+iY')\uparrow\rangle$	$E_0'-E_0+\Delta_0$
	$\frac{1}{2}\lvert(X'+iY')\downarrow\rangle$	$E_0'-E_0+\Delta_0$
	$\sqrt{\frac{2}{3}}\lvert Z'\uparrow\rangle-\frac{1}{\sqrt{6}}\lvert(X'+iY')\downarrow\rangle$	$E_0'-E_0+\Delta_0$
	$\sqrt{\frac{2}{3}}\lvert Z'\downarrow\rangle+\frac{1}{\sqrt{6}}\lvert(X'+iY')\uparrow\rangle$	$E_0'-E_0+\Delta_0$
Γ_{7c}	$-\frac{1}{\sqrt{3}}\lvert Z'\uparrow\rangle-\frac{1}{\sqrt{3}}\lvert(X'+iY')\downarrow\rangle$	$E_0'-E_0$
	$\frac{1}{\sqrt{3}}\lvert Z'\downarrow\rangle-\frac{1}{\sqrt{3}}\lvert(X'+iY')\uparrow\rangle$	$E_0'-E_0$

TABLE I. Basis functions and energies for 14-band $\vec{k}\cdot\vec{p}$ model [8].

elements are given by

$$\begin{aligned}
P_0 &= h'\langle S\sigma|\,p_x\,|X\sigma\rangle = h'\langle S\sigma|\,p_x\,|Y\sigma\rangle \\
&= h'\langle S\sigma|\,p_x\,|Z\sigma\rangle\,, \\
P_1 &= ih'\langle X'|\,p_x\,|S\rangle = ih'\langle Y'|\,p_y\,|S\rangle = ih'\langle Z'|\,k_z\,|S\rangle\,, \\
Q &= h'\langle X|\,p_y\,|Z'\rangle = -h'\langle X|\,p_y\,|Z'\rangle\,, \\
\Delta^- &= -\tfrac{3h'}{4m_*}\langle X|\,[(\nabla V_0)\times p]_y\,|Z'\rangle \\
&= \tfrac{3h'}{4m_*}\langle Z|\,[(\nabla V_0)\times p]_y\,|X'\rangle
\end{aligned}$$

with $h' = \hbar/m_0$ and $m_* = m_0c^2$. These elements can be taken as phenomenological parameters that can be determined experimentally. From these values, the Hamiltonian for the system can be constructed as a 14×14 matrix, which is given explicitly in Appendix A.

To adapt this Hamiltonian to account for the effects of mechanical strain on the system, we follow Pikus and Bir [27]. The method consists of adding an extra term to each element of the unstrained Hamiltonian created by replacing k_xk_y (and it's circular permutations) with the component of the strain tensor ϵ_{xy} and the Luttinger parameters with deformation potentials. Thus, the total system Hamiltonian is given by $H = H_0 + H_\epsilon$. H_ϵ is given explicitly in Appendix B. As the influence of strain on the p-type conduction bands (Γ_{7c} and Γ_{8c}) is currently unknown, the p-type conduction band hydrostatic deformation potential ($a_{\Gamma_{7c}}$ and $a_{\Gamma_{8c}}$) and p-type CB shear deformation potential ($b_{\Gamma_{7c}}$ and $b_{\Gamma_{8c}}$) are neglected. The results of our bandstructure calculations for different levels and types of strain are shown Fig. 15.

Finally, with the parameters gained from these calculations, we estimate the Dresselhaus and Rashba constants based on Eqs. (13) and (14),

$$\begin{aligned}
\beta = \frac{4P_0P_1Q}{3}&\left[\frac{1}{E_0G_0}-\frac{1}{(E_0+\Delta_0)(G_0+\Delta_0')}\right] \\
&-\frac{4P_0^2Q\Delta^-}{9E_0(E_0+\Delta_0)}\left[\frac{2}{G_0}+\frac{1}{G_0+\Delta_0'}\right] \\
&-\frac{4P_1^2Q\Delta^-}{9G_0(G_0+\Delta_0')}\left[\frac{1}{E_0}+\frac{2}{E_0+\Delta_0}\right],
\end{aligned} \tag{13}$$

$$\begin{aligned}
\eta = \frac{1}{3}&\left[\frac{P_0^2}{(E_0+\Delta_0)^2}-\frac{P_0^2}{E_0^2}+\frac{P_1^2}{G_0^2}-\frac{P_1^2}{(G_0+\Delta_0')^2}\right]\frac{\mathrm{d}V_{ext}}{\mathrm{d}y} \\
&-\frac{2P_1P_0\Delta^-}{9}\left[\frac{1}{E_0(G_0+\Delta_0')^2}-\frac{1}{E_0^2(G_0+\Delta_0')}\right. \\
&\left.-\frac{2}{G_0(E_0+\Delta_0)^2}+\frac{2}{G_0^2(E_0+\Delta_0)}\right]\frac{\mathrm{d}V_{ext}}{\mathrm{d}y}
\end{aligned} \tag{14}$$

and by extension the change in spin-orbit coupling with respect to mechanical strain.

B. Spin-Orbit Coupling of Strained Device

We integrate the method presented in the previous section with our simulation techniques to include the effects of mechanical strain by first conducting $\vec{k}\cdot\vec{p}$ calculations for compressive strain in the [001], [110] and [111] crystallographic directions. This is achieved by taking a small change in the lattice spacing a_s of between 0 and 4 percent of the unstrained lattice constant a_0. With this we have calculated the strain in the direction of the applied force as $e_\parallel = \frac{a_s}{a_0} - 1$ and the strain in the perpendicular direction as $e_\perp = -D_{[hkl]}e_\parallel$ where h, k and l are the Miller indices for the direction of the strain. The direction of the strain has been then accounted for by modifying the strain tensor e_{hkl} as follows

$$e_{001} = \begin{pmatrix} e_1 & 0 & 0 \\ 0 & e_1 & 0 \\ 0 & 0 & e_1 \end{pmatrix}, \tag{15}$$

$$e_{111} = \begin{pmatrix} e_2 & e_3 & e_3 \\ e_3 & e_2 & e_3 \\ e_3 & e_3 & e_2 \end{pmatrix}, \tag{16}$$

$$e_{110} = \begin{pmatrix} e_4 & e_5 & 0 \\ e_5 & e_4 & 0 \\ 0 & 0 & e_1 \end{pmatrix}, \tag{17}$$

where

$$e_1 = e_\parallel, \tag{18a}$$
$$e_2 = \tfrac{1}{3}(e_\perp + 2e_\parallel), \tag{18b}$$
$$e_3 = \tfrac{1}{3}(e_\perp - e_\parallel), \tag{18c}$$
$$e_4 = \tfrac{1}{2}(e_\perp + e_\parallel), \tag{18d}$$
$$e_5 = \tfrac{1}{2}(e_\perp + e_\parallel) \tag{18e}$$

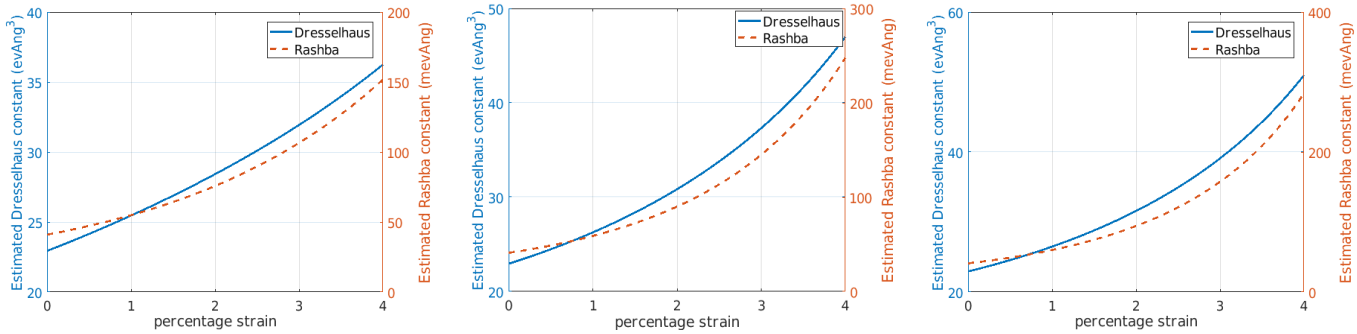

(a) Strain in direction [001]. (b) Strain in direction [110]. (c) Strain in direction [111].

FIG. 16. Spin-orbit coupling constants η and β as a function of strain ranging from 0% to 4% for three different strain directions. η has been calculated for $V_g = 0.9\,\mathrm{V}$ corresponding to an average electric field of $3.6 \times 10^8\,\mathrm{V/m}$.

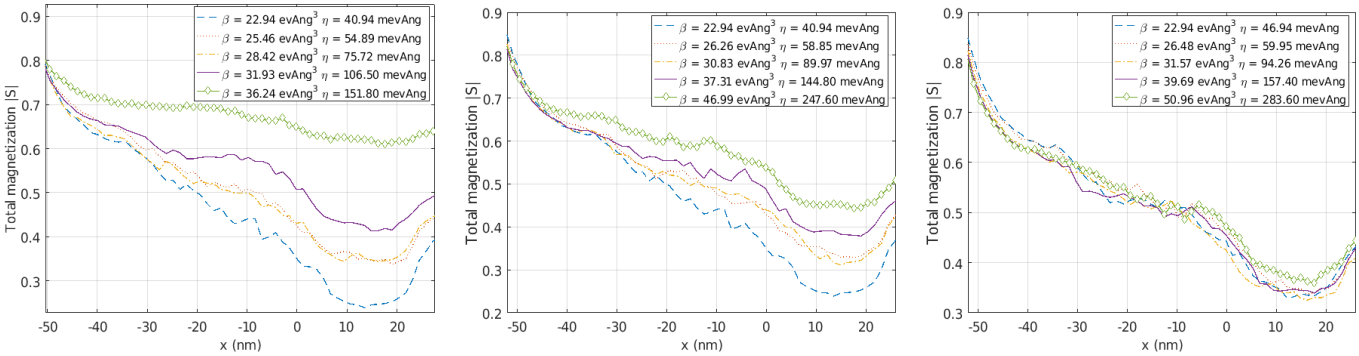

(a) Strain in direction [001]. (b) Strain in direction [110]. (c) Strain in direction [111].

FIG. 17. Magnetization along the device channel vs. strain ranging from 0% to 4% for three different strain directions, taken after a steady state was reached at $t = 8\,\mathrm{ps}$ for a gate and source-drain voltage of $0.9\,\mathrm{V}$ for x-injection for indicated Dresselhaus (β) and Rashba (η) spin-orbit coupling constants.

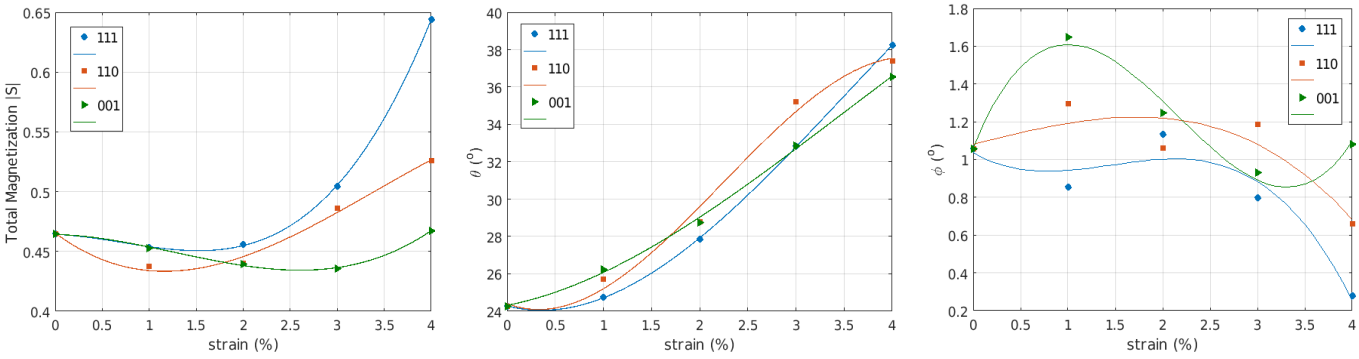

(a) Total magnetization at drain (b) Azimuthal angle at drain (c) Elevation angle at drain

FIG. 18. Steady state magnetization at drain as a function of strain along different axis (x-injection, $V_D = V_G = 0.9\,\mathrm{V}$) with nonlinear spline fits to serve as a guide to the eye in elucidating trends in the data.

and the coefficients $D_{[hkl]}$ are given by

$$D_{[001]} = \frac{2C_{12}}{C_{11}}, \tag{19a}$$

$$D_{[110]} = \frac{C_{11} + 3C_{12} - 2C_{44}}{C_{11} + C12 + 2C44}, \tag{19b}$$

$$D_{[111]} = \frac{2C_{11} + 4C_{12} - 4C_{44}}{C_{11} + 2C12 + 4C44}. \tag{19c}$$

From this, we extract the new inter-band energies for the strained system E_0' and E_1' (by extension G_0' and G_1') and use these to calculate the change in spin-orbit coupling parameters β and η via Eqs. (13) and (14). Finally, these new constants are inserted into our Monte Carlo simulation to investigate the effects of strain on the spin transport across the device.

C. Effect of Strain on Magnetization

Fig. 16 shows the results for the Dresselhaus and Rashba spin-orbit coupling constants. Both increase non-linearly with strain due to the change in energy gap between the Γ_{6c} and Γ_{7v} bands at the Gamma point E_0. The results of using these constants with the overall Monte Carlo simulations for the MOSFET device introduced in Section III are shown in Fig. 17. We see that the direction and strength of the strain has a direct impact on the amount of decay and recovery seen at the drain.

For strain in the [001] direction with S_x injection (Fig. 17a), a steady decrease in magnetization occurs when moving from the source to the drain, although at lower rates for stronger strain, with a recovery of magnetization at the drain. With increasing strain the magnetization at the drain increases from a value of 0.36 in the unstrained case to 0.64 for 4.0% strain. It should be noted, however, that the rate of spin recovery appears to decrease with increasing strain. The unstrained case gives rise to an increase in magnetization of 0.13 from the lowest value whilst 4.0% strain gives rise to a recovery of only 0.02 from the lowest value. The increased magnetization at the drain is likely due to the decrease in the overall decay.

Fig. 17b shows similar results for strain in the [110] direction. An increase in strain leads to a decrease in the amount of magnetization decay across the channel and an increase at the drain. Again, much like the previous case, the rate of recovery decreases with increasing strain, with the unstrained case yielding a recovery of 0.13 whilst the 4.0% case only yields a recovery of 0.07.

The result is notably different for increasing strain in the [111] direction, shown in Fig. 17c. The increased spin-orbit coupling in this case has little effect on the total magnetization at the drain edge as the differences between the curves fall within the variance of the simulations. The magnetization still recovers at the drain, roughly by the same amount of 0.13.

Fig. 18a shows the total magnetization at the drain as a function of strain for different strain directions, showing a non-linear increase for strain in the [001] and [110] directions, but no significant variation for strain in the [111] direction. Fig. 18c, showing small fluctuations of the elevation angle ϕ around 1° for all three strain directions, suggests that the elevation angle ϕ is not significantly affected by strain. Fig. 18b, however, shows a non-linear increase of the azimuthal rotation angle θ with strain for all strain directions, including the [111] direction, which shows no significant change in the total drain magnetization for increasing strain. This suggests that the azimuthal rotation angle of the magnetization vector may be the best measure of overall strain.

V. CONCLUSIONS

Ensemble Monte Carlo device simulations of electron-spin transport across a realistic structure of a 25 nm gate length $In_{0.3}Ga_{0.7}As$ MOSFET show that the total magnetization and orientation of the magnetization (represented by the length and direction of the Bloch vector associated with the spin degrees of freedom) can be controlled via the gate voltage. We also observe a spin recovery between the gate and the drain, which may be due to a spin refocusing effect induced by the high electric fringing field at the gate [14]. If experimentally verified, this recovery could be exploited in devices to counter the spin decay that such devices would otherwise suffer.

We also investigated the effects of mechanical strain on the evolution of the magnetization showing that the spin transport is sensitive to strain; larger strain leads to reduced magnetization decay when moving across the channel, dependent on the strain direction. The magnetization vector also undergoes a coherent rotation between the source and the drain due to spin-orbit coupling. Significantly, the azimuthal rotation angle exhibits a non-linear increase with the amount of strain for all strain directions. This effect has the potential for use in an electronic molecular-strain sensor as, in principle, injecting polarized spins into the channel and monitoring magnetization at the drain provides an indirect measure of strain acting on the device channel.

ACKNOWLEDGMENTS

This research was funded by the Sêr Cymru National Research Network for Advanced Engineering and Materials (grant NRN 082). SS also acknowledges funding from a Royal Society Leverhulme Trust Senior Research Fellowship. We would like to thank Jaroslav Fabian (Regensburg University) for helpful comments and suggestions.

Appendix A: Hamiltonian for Extended Kane Model

The Hamiltonian H_0 for the 7-band system described in Section IV A is given by the matrix [24, 28]

$$H_0 = \begin{pmatrix} H_c & H_{cv} & H_{cc'} \\ H_{vc} & H_v & H_{vc'} \\ H_{c'c} & H_{c'v} & H_{c'} \end{pmatrix}. \tag{A1}$$

Setting $E_v = V(r) - E_0$, $E_{c'} = V(r) + E_0'$ and $k_\pm = k_x \pm ik_y$, $H_{cc'}$ and $H_{c'v}$ are obtained by the transposition of $H_{c'c}$ and $H_{vc'}$, respectively, with the following substitutions: $k_\pm \to k_\mp$, $P_1 \to -P_1$, $Q \to -Q$ and

$\Delta^- \to -\Delta^-$, where

$$D = \tfrac{\hbar^2\gamma_1}{2m_0}(k_x^2+k_y^2+k_z^2), \tag{A2a}$$
$$G = \tfrac{\hbar^2\gamma_2}{2m_0}(k_x^2+k_y^2-2k_z^2), \tag{A2b}$$
$$S = \tfrac{\hbar^2\gamma_3}{m_0}\sqrt{3}(k_x-ik_y)k_z, \tag{A2c}$$
$$R = \tfrac{\hbar^2}{2m_0}\left[-\sqrt{3}\gamma_2(k_x^2-k_y^2)+i2\sqrt{3}\gamma_3 k_x k_y\right]. \tag{A2d}$$

The elements of Eq. (A1) are

$$H_c = \begin{pmatrix} \frac{\hbar^2k^2}{2m_0}+V(r) & 0 \\ 0 & \frac{\hbar^2k^2}{2m_0}+V(r) \end{pmatrix}, \tag{A3a}$$

$$H_{vc} = \frac{1}{\sqrt{6}}\begin{pmatrix} -\sqrt{3}P_0k_- & 0 \\ 2P_0k_z & -P_0k_- \\ P_0k_+ & 2P_0k_z \\ 0 & \sqrt{3}P_0k_+ \\ -\sqrt{2}P_0k_z & -\sqrt{2}P_0k_- \\ 7-\sqrt{2}P_0k_+ & \sqrt{2}P_0k_z \end{pmatrix}, \tag{A3b}$$

$$H_{cv} = \begin{pmatrix} -\frac{1}{\sqrt{2}}P_0k_+ & \sqrt{\frac{2}{3}}P_0k_z & \frac{1}{\sqrt{6}}P_0k_- & 0 & -\frac{1}{\sqrt{3}}P_0k_z & -\frac{1}{\sqrt{3}}P_0k_- \\ 0 & -\frac{1}{\sqrt{6}}P_0k_+ & \sqrt{\frac{2}{3}}P_0k_z & \frac{1}{\sqrt{2}}P_0k_- & -\frac{1}{\sqrt{3}}P_0k_+ & -\frac{1}{\sqrt{3}}P_0k_z \end{pmatrix}, \tag{A3c}$$

$$H_{cc'} = \begin{pmatrix} -\frac{i}{\sqrt{2}}P_1k_+ & i\sqrt{\frac{2}{3}}P_1k_z & \frac{i}{\sqrt{6}}P_1k_- & 0 & -\frac{i}{\sqrt{3}}P_1k_z & -\frac{i}{\sqrt{3}}P_1k_- \\ 0 & -\frac{i}{\sqrt{6}}P_1k_+ & i\sqrt{\frac{2}{3}}P_1k_z & \frac{i}{\sqrt{2}}P_1k_- & -\frac{i}{\sqrt{3}}P_1k_+ & \frac{i}{\sqrt{3}}P_1k_z \end{pmatrix}, \tag{A3d}$$

$$H_v = \begin{pmatrix} (D+G)+E_v & 0 & -S & R & -\frac{S}{\sqrt{2}} & \sqrt{2}R \\ 0 & (D+G)+E_v & R^+ & S^+ & -\sqrt{2}R^+ & -\frac{S^+}{\sqrt{2}} \\ -S^+ & R & (D-G)+E_v & S & -\sqrt{2}G & \sqrt{\frac{3}{2}}S \\ R^+ & S & S^+ & (D-G)+E_v & \sqrt{\frac{3}{2}}S^+ & \sqrt{2}G \\ \frac{-S^+}{\sqrt{2}} & -\sqrt{2}R & -\sqrt{2}G^+ & \sqrt{\frac{3}{2}}S & D+E_v-\Delta_0 & 0 \\ \sqrt{2}R & \frac{-S}{\sqrt{2}} & \sqrt{\frac{3}{2}}S^+ & \sqrt{2}G^+ & 0 & D+E_v-\Delta_0 \end{pmatrix}, \tag{A3e}$$

$$H_{vc'} = \begin{pmatrix} \frac{i}{3}\Delta^- & \frac{i}{\sqrt{3}}Qk_+ & \frac{i}{\sqrt{3}}Qk_z & 0 & -\frac{i}{\sqrt{6}}Qk_+ & -i\sqrt{\frac{2}{3}}Qk_z \\ -\frac{i}{\sqrt{3}}Qk_- & \frac{i}{3}\Delta^- & 0 & \frac{i}{\sqrt{3}}Qk_z & 0 & \frac{i}{\sqrt{2}}Qk_+ \\ -\frac{i}{\sqrt{3}}Qk_z & 0 & \frac{i}{3}\Delta^- & -\frac{i}{\sqrt{3}}Qk_+ & -\frac{i}{\sqrt{2}}Qk_- & 0 \\ 0 & -\frac{i}{\sqrt{3}}Qk_z & \frac{i}{\sqrt{3}}Qk_- & \frac{i}{3}\Delta_- & -i\sqrt{\frac{2}{3}}Qk_z & \frac{i}{\sqrt{6}}Qk_- \\ \frac{i}{\sqrt{6}}Qk_- & 0 & \frac{i}{\sqrt{2}}Qk_+ & i\sqrt{\frac{2}{3}}Qk_z & -\frac{2i}{3}\Delta^- & 0 \\ i\sqrt{\frac{2}{3}}Qk_z & -\frac{i}{\sqrt{2}}Qk_- & 0 & -\frac{i}{\sqrt{6}}Qk_+ & 0 & -\frac{2i}{3}\Delta^- \end{pmatrix}, \tag{A3f}$$

$$H_c' = \begin{pmatrix} \frac{\hbar^2\mathbf{k}^2}{2m_0}+E_{c'}+\Delta_0' & 0 & 0 & 0 & 0 & 0 \\ 0 & \frac{\hbar^2\mathbf{k}^2}{2m_0}+E_{c'}+\Delta_0' & 0 & 0 & 0 & 0 \\ 0 & 0 & \frac{\hbar^2\mathbf{k}^2}{2m_0}+E_{c'}+\Delta_0' & 0 & 0 & 0 \\ 0 & 0 & 0 & \frac{\hbar^2\mathbf{k}^2}{2m_0}+E_{c'}+\Delta_0' & 0 & 0 \\ 0 & 0 & 0 & 0 & \frac{\hbar^2\mathbf{k}^2}{2m_0}+E_{c'} & 0 \\ 0 & 0 & 0 & 0 & 0 & \frac{\hbar^2\mathbf{k}^2}{2m_0}+E_{c'} \end{pmatrix}. \tag{A3g}$$

The γ_i represent modified Luttinger parameters from which the $\vec{k}\cdot\vec{p}$ interaction of the Γ_{8v} level with the Γ_{6c}, Γ_{8c} and Γ_{7c} levels has been subtracted since the interaction is included explicitly in the matrix. The γ_i are given by

$$\gamma_1 = \gamma_1^L + \frac{E_{p_0}}{3E_0} - \frac{E_Q}{3(E_0'-E_0)} - \frac{E_Q}{3(E_0'-E_0+\Delta_0')}, \tag{A4a}$$

$$\gamma_2 = \gamma_2^L + \frac{E_{p_0}}{6E-0} - \frac{E_Q}{6(E_0'-E_0)}, \tag{A4b}$$

$$\gamma_3 = \gamma_3^L + \frac{E_{p_0}}{6E-0} - \frac{E_Q}{6(E_0'-E_0)}. \tag{A4c}$$

Appendix B: Bir and Pikus Strain Hamiltonian

The strain Hamiltonian H_ϵ for the seven band system described in Section IV A is given by [27, 28]

$$H_\epsilon = \begin{pmatrix} H_c & H_{cv} & 0_{2\times6} \\ H_{vc} & H_v & 0_{6\times6} \\ 0_{6\times2} & 0_{6\times6} & 0_{6\times6} \end{pmatrix} \tag{B1}$$

where $H_{vc} = H_{cv}^\dagger$. Setting $A_\epsilon = a_c(\epsilon_{xx}+\epsilon_{yy}+\epsilon_{zz})$, $v = \frac{P_0}{\sqrt{6}}\sum_j(\epsilon_{xj} - i\epsilon_{yj})$ and $u = \frac{P_0}{\sqrt{3}}\sum_j \epsilon_{zj}$ we have

$$H_c = \begin{pmatrix} A_\epsilon & 0 \\ 0 & A_\epsilon \end{pmatrix},$$

$$H_{cv} = \begin{pmatrix} \sqrt{3}v^\dagger & -\sqrt{2}u & -v & 0 & -u & -\sqrt{2}v \\ 0 & v^\dagger & -\sqrt{2}u & -\sqrt{3}v & \sqrt{2}v^\dagger & u \end{pmatrix}$$

and setting

$$\begin{aligned} D_\epsilon &= -a_v(\epsilon_{xx}+\epsilon_{yy}+\epsilon_{zz}), \\ G_\epsilon &= -b(\epsilon_{xx}+\epsilon_{yy}-2\epsilon_{zz})/2, \\ S_\epsilon &= -d(\epsilon_{xz}-i\epsilon_{yz}), \\ R_\epsilon &= \tfrac{\sqrt{3}}{2}b(\epsilon_{xx}-\epsilon_{yy}) - id\epsilon_{xy} \end{aligned}$$

we have

$$H_v = \begin{pmatrix} (D_\epsilon+G_\epsilon) & 0 & -S_\epsilon & R_\epsilon & -\frac{S_\epsilon}{\sqrt{2}} & \sqrt{2}R_\epsilon \\ 0 & (D_\epsilon+G_\epsilon) & R_\epsilon^\dagger & S_\epsilon^\dagger & -\sqrt{2}R_\epsilon^\dagger & -\frac{S_\epsilon^\dagger}{\sqrt{2}} \\ -S_\epsilon^\dagger & R_\epsilon & (D_\epsilon-G_\epsilon) & S_\epsilon & -\sqrt{2}G_\epsilon & \sqrt{\frac{3}{2}}S_\epsilon \\ R_\epsilon^\dagger & S_\epsilon & S_\epsilon^\dagger & (D_\epsilon-G_\epsilon) & \sqrt{\frac{3}{2}}S_\epsilon^\dagger & \sqrt{2}G_\epsilon \\ \frac{-S_\epsilon^\dagger}{\sqrt{2}} & -\sqrt{2}R_\epsilon & -\sqrt{2}G_\epsilon^\dagger & \sqrt{\frac{3}{2}}S_\epsilon & D_\epsilon-\Delta_0 & 0 \\ \sqrt{2}R_\epsilon & \frac{-S_\epsilon}{\sqrt{2}} & \sqrt{\frac{3}{2}}S_\epsilon^\dagger & \sqrt{2}G_\epsilon^\dagger & 0 & D_\epsilon-\Delta_0 \end{pmatrix}.$$

[1] D. D. Awschalom, L. C. Bassett, A. S. Dzurak, E. L. Hu, and J. R. Petta, Science **339**, 1174 (2013).
[2] S. Wolf, D. D. Awschalom, R. A. Buhrman, J. M. Daughton, S. von Molinár, M. L. Roukes, A. Y. Chtchelkanova, and D. M. Treger, Science **294**, 1488 (2001).
[3] S. Datta and B. Das, Applied Physics Letters **56**, 665 (1990).
[4] S. Sugahara and M. Tanaka, Aplied Physics Letters **84**, 2307 (2004).
[5] "International technology roadmap for semiconductors (ITRS)," `http://www.itrs2.net/2013-itrs.html` (2013).
[6] W. Y. Choi, H. Kim, J. Chang, S. H. Han, H. C. Koo, and M. Johnson, Nat Nano **10**, 666 (2015).
[7] S. D. Sarma, American Scientist **89**, 516 (2001).
[8] J. Fabian, A. Matos-Abiague, C. Ertler, P. Stano, and I. Zutic, Acta Physica Slovaca **54**, 565 (2007).
[9] J. Schliemann, J. C. Egues, and D. Loss, Phys. Rev. Lett. **90**, 146801 (2003).
[10] K. Kalna, N. Seoane, A. J. Garca-Loureiro, I. G. Thayne, and A. Asenov, IEEE Trans. Electron Devices **55**, 2297 (2008).
[11] N. Seoane, M. Aldegunde, D. Nagy, M. A. Elmessary, G. Indalecio, A. J. Garca-Loureiro, and K. Kalna, Semiconductor Science and Technology **31**, 075005 (2016).
[12] K. Tomizawa, *Numerical Simulation of Submicron Semiconductor Devices* (Artech House, 1993).
[13] D. K. Ferry, Superlattices and Microstructures **27**, 61 (2000).
[14] A. Islam, B. Benbakhti, and K. Kalna, IEEE Trans. Nanotechnology **10**, 1424 (2011).
[15] K. Kalna, S. Roy, A. Asenov, K. Elgaid, and I. Thayne, Solid-St. Electron. **46**, 331 (2002).
[16] D. A. J. Moran, K. Kalna, E. Boyd, F. McEwan, H. McLelland, L. Zhuang, C. R. Stanley, A. Asenov, and I. Thayne, in *Proc. 29th ESSDERC* (2003) pp. 315–318.
[17] K. Kalna, K. Elgaid, I. Thayne, and A. Asenov, in *Proc. 17th Indium Phosphide Related Materials* (2005) pp. 61–65.
[18] B. Benbakhti, A. Martinez, K. Kalna, G. Hellings, G. Eneman, K. D. Meyer, and M. Meuris, IEEE Trans. Nanotechnoogy. **11**, 808 (2012).
[19] M. Shen, S. Saikin, M.-C. Cheng, and V. Privman, Mathematics and Computers in Simulation **65**, 351 (2004).
[20] M. Cardona, N. E. Christensen, and G. Fasol, Physical Review B **38**, 1806 (1988).

[21] R. Neffati, I. Saidi, and K. Boujdaria, J. Applied Physics **112**, 053716 (2012).
[22] E. O. Kane, J. Phys. Chem. Solids **1**, 249 (1957).
[23] P. Pfeffer and W. Zawadzki, Physical Review B **41**, 1561 (1990).
[24] P. Pfeffer and W. Zawadzki, Physical Review B **53**, 12813 (1996).
[25] J. M. Luttinger and W. Kohn, Physical Review **97**, 869 (1955).
[26] P. Lowdin, J. Chemial Physics **19**, 1396 (1951).
[27] S. L. Chuang, *Physics of Optoelectronic Devices*, edited by J. W. Goodman (John Wiley & Sons Inc., 1995).
[28] T. B. Bahder, Physical Review B **41**, 11992 (1990).